Cloud Fluctuation Statistics

R. F. CAHALAN, D. A. SHORT AND G. R. NORTH

Laboratory for Atmospheric Sciences, NASA/Goddard Space Flight Center, Greenbelt, MD 20771

(Manuscript received 16 April 1981, in final form 4 December 1981)

ABSTRACT

A space-time statistical analysis of total outgoing infrared radiation (derived from the 10.5–12.5 μm window measurements of the NOAA operational satellites) is used to determine the gross features of day-to-day cloudiness fluctuations over the Pacific Ocean in summer and winter. Infrared fluctuations arise from the passage of cloudiness systems through a grid box as well as the creation and destruction of cloudiness in the box. Which process dominates depends upon the size of the box relative to the size, speed and persistence time of a typical cloudiness system. In most regions the statistical analysis yields advection speeds characteristic of 700 mb mean flow with spatial dependence resembling the 300 mb mean flow. Spatial scales less than 2000 km predominate, smaller scales having less persistence. Characteristic time scales are on the order of one or two days, even for a grid box spanning the entire North Pacific storm track. This result is remarkable in view of the much longer time scales commonly associated with atmospheric disturbances. Apparently many cloudiness systems are created and destroyed during the lifetime of a single disturbance.

1. Introduction

Fluctuations in cloudiness provide an obvious manifestation of atmospheric variability, both in small-scale hourly changes seen from a point on the earth's surface and in large-scale longer period changes evident from space. Yet the treatment of cloudiness remains the greatest source of uncertainty in models of the atmosphere and its climate. Difficulties arise for two reasons: First, cloudiness is produced by a poorly understood interaction of small-scale turbulent convective processes and large-scale flow. Second, cloudiness produces large changes in absorbed solar and outgoing infrared radiation, resulting in changes in net radiation. Both problems affect estimates of climate sensitivity, since one must know how cloudiness changes under a given perturbation, as well as whether the change produces a positive or negative feedback.

Aside from their intrinsic climatological interest we wish to study the space and time scales of cloudiness for the following reasons:

1) These early crude estimates from the existing operational satellite data will aid in the design of future experiments having the space and time sampling necessary to secure minimum coverage for climate monitoring purposes (King and Curran, 1980).

2) Knowing the space and time scales allows us to determine the standard error associated with estimating climatic (ensemble mean) cloudiness in some region by averaging cloudiness over a particular area and time period (Leith, 1973). This is helpful in deciding whether an anomaly in average cloudiness is part of the natural variability of climate or represents a change in climatic regime.

3) The large general circulation models (GCM's) have reached the point in their evolution that cloudiness at various levels is being dynamically computed and allowed to feedback on the system. Hence, there is an urgent need for cloudiness statistics in order to test and calibrate the models.

4) We wish to re-emphasize the last point by noting that some recent theoretical considerations (Leith, 1975; Bell, 1980; North, *et al.*, 1981) suggest that the ability of a climate model to estimate time-lagged statistics may be closely related to its ability to estimate climate sensitivity.

5) Finally, there always exists the hope that the statistics will be so simple (such as white noise) that we can take some advantage and construct climate models simpler than GCM's (North and Cahalan, 1981).

This paper examines the statistical features of day-to-day fluctuations in total outgoing infrared radiation (IR). The IR fluctuations are dominated by cloudiness particularly where cloud tops are substantially higher than the boundary layer. [In low cloudiness regions water vapor can be important (see, for example, Roberts *et al.*, 1976 and Coffey, 1977).] We focus on the Pacific Ocean, where the diurnal cycle is relatively small, and we determine charac-

teristic times and spatial scales of the IR fluctuations for both summer and winter seasons. Characteristic times tend to increase as the averaging area increases, but they reach a limit for sufficiently large averaging areas. This effect is explained by the advection of cloudiness, which reduces autocorrelation times at single gridpoints. Similar advecting correlations are encountered in wind-tunnel turbulence experiments (Schlichting, 1968). The advection of cloudiness correlations unfortunately depends in an unknown way on the vertical cloudiness distribution. In most regions we find speeds typical of 700 mb flow with spatial dependence resembling the 300 mb flow in summer and winter.

The outline of the paper is as follows: In the remainder of this section we first summarize previous work on IR fluctuations and then give a schematic summary of our own results. The following section describes the data base. Section 3 presents the means, standard deviations and time-lag autocorrelation functions of individual grid point and areal average IR signals. Section 4 examines the cross correlations between the signal at some chosen grid point and simultaneous and time-lagged signals at other points. This provides a Lagrangian picture helpful in interpreting the Eulerian time scales of the preceding section. Section 5 gives a brief discussion of results. The Appendix provides a simplified derivation of the relationship between the Eulerian time scales of Section 3 and the Lagrangian time scales of Section 4.

Previous studies which have used NOAA scanning radiometer data are numerous as well as varied in their motivations and analysis techniques. The simultaneous 0900 local time (LT) measurements of albedo and outgoing IR have been used extensively to infer the net radiative heating of the earth-atmosphere system (see Winston and Krueger, 1977, for example). An analysis of the correlation between variations in albedo and outgoing IR (on monthly and daily time scales) has been used to estimate the effect of cloudiness changes on the radiation budget of the earth (Ohring and Clapp, 1980; Hartmann and Short, 1980). In his study of cyclogenesis over the North Pacific in winter Reed (1979) used NOAA IR operational images to pinpoint the location of cloud development produced by intensifying tropospheric disturbances. Riehl and Miller (1978) and Short and Wallace (1980) examined the morning-to-evening difference in outgoing IR and found it to be dominated by changes in cloudiness and surface temperature, especially over land. Heddinghaus and Krueger (1981), using an empirical orthogonal function (EOF) analysis on the monthly means, have found the annual cycle to be dominated by the Northern Hemisphere continents with the largest interannual variability over the tropical Pacific Ocean in phase with the Southern Oscillation. Murakami (1980a,b,c) used an EOF analysis in order to examine various temporal scales of IR fluctuations during the winter and summer monsoon seasons over the tropical western Pacific.

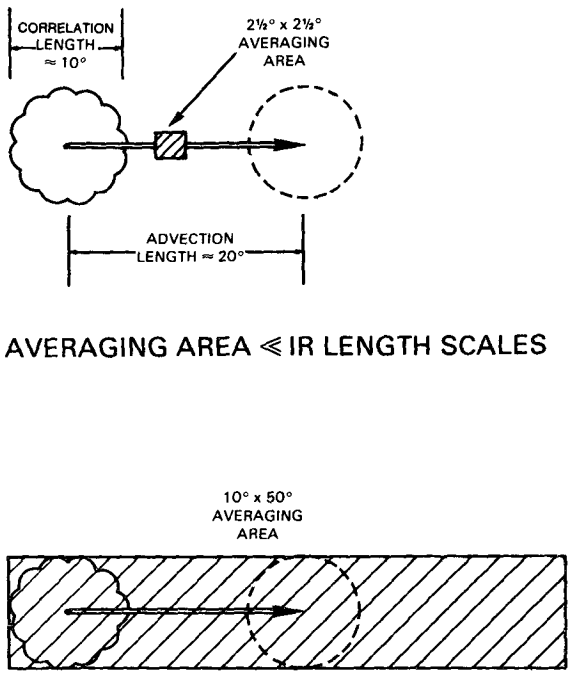

FIG. 1. Schematic view of midlatitude winter infrared fluctuations.

In summarizing the present study we introduce some terminology useful in describing the statistics of large-scale fluctuating cloudiness. A cloudiness system contains a wide spectrum of length scales and produces correlations between IR at separate gridpoints which tend to decrease with distance. The system therefore consists of a number of statistically independent subsystems, the size of which is determined by the correlation diameter, defined as twice the separation between gridpoints required for simultaneous IR signals at the two points to have a correlation of $1/e$. Each subsystem is not only uncorrelated with the others, but also becomes uncorrelated with itself as it advects across a region. The signal at a fixed gridpoint therefore has an autocorrelation which decays with lag time because of advection of uncorrelated subsystems past the gridpoint and because of the decay of correlation within each subsystem. The Eulerian correlation time is defined as the lag time required for the autocorrelation of a fixed gridpoint or area averaged signal to fall to $1/e$. Due to advection, the signal at a given point is more correlated with time-lagged signals at points downstream. The Lagrangian correlation time is de-

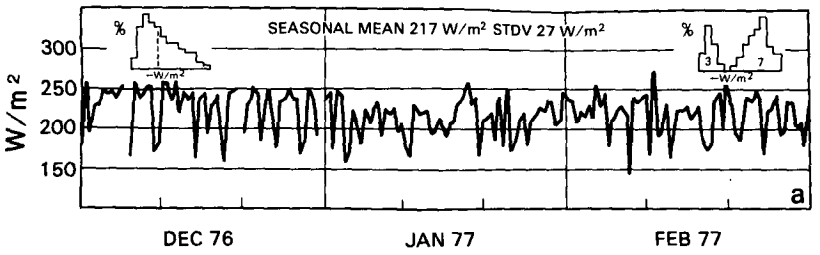

FIG. 2a. Time series of outgoing IR in winter (DJF) for a single gridpoint at 40°N, 180°. Insert at left is a frequency distribution for all four winters with higher values on the left. Insert at right is the product of the frequency and the squared deviations from the mean. Seventy percent of the variance is accounted for by deviations below the mean.

fined as the lag time required for the maximum downstream correlation to fall to $1/e$. The advection length associated with the given point is defined as the distance to this downstream $1/e$ maximum.

Values of the above quantities typical of the North Pacific winter storm track are schematically illustrated in Fig. 1. The 2½° × 2½° shaded square in Fig. 1a represents the averaging area of a typical gridpoint, while the 10° × 50° shaded region in Fig. 1b represents an average over the entire Pacific region. In Section 3 we show that the Eulerian correlation times increase with averaging area, from less than 12 h for midlatitude gridpoints to ~24 h for the entire storm track region. In Section 4 we show that these time scales are associated with the advection of cloudiness subsystems, indicated by circular regions in Fig. 1, which have a correlation diameter of ~10°, a Lagrangian correlation time of ~24 h, and an advection length of ~20°. The fact that the Lagrangian time and the large area Eulerian times are equal is derived in the Appendix from a simple "cloud dot" model.

2. Data and analysis technique

The data utilized in this study originate from measurements of outgoing infrared radiation (IR) in the 10.5–12.5 μm atmospheric window taken by the scanning radiometer aboard the NOAA operational satellites. The polar orbiting NOAA system provides global coverage of outgoing IR twice daily (0900 and 2100 LT) with 45 consecutive months of data currently available. The total outgoing IR data set analyzed here was derived from these window measurements (for details see Gruber and Winston, 1978) and was provided to us by the Environmental Data and Information Service of NOAA on a 2½° × 2½° latitude/longitude grid.

We have divided the data set into four winter seasons (DJF) and four summer seasons (JJA) which span the period from June 1974 to February 1978. We have furthermore concentrated on a sector of the Pacific Ocean, 120° in longitude centered on the dateline. This sector is convenient for our analysis since the seasonal cycle is small over the Pacific, so that single season time series such as those shown in Fig. 2 (see Section 3) are approximately stationary. The seasonal cycle is significant over the land included in the 120° sector, and has been removed by a least squares quadratic fit.

Day-to-day deviations from the seasonal value of the total outgoing IR at any given point p constitute a stationary time series $s(\mathbf{p}, t)$ having zero seasonal mean. From the time series at two chosen points $\mathbf{p}_1$ and $\mathbf{p}_2$ one can determine the space-time correlation function, given by (see for example Gandin, 1963)

$$\rho(\mathbf{p}_1, \mathbf{p}_2; \tau) \equiv \overline{s(\mathbf{p}_1, t)s(\mathbf{p}_2, t+\tau)}/(\sigma_1\sigma_2), \quad (1)$$

where the bar indicates a seasonal time average, τ is a time lag, and σ_1 and σ_2 are the standard deviations at the two points. An advantage to studying (1) directly rather than computing spatial spectra is that we avoid any initial assumptions of homogeneity or isotropy, and can therefore look for evidence of the preferred location and orientation of cloud bands.

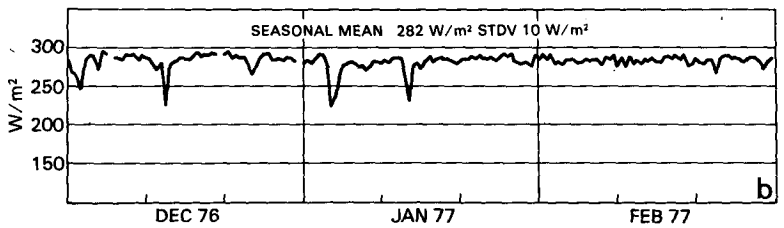

FIG. 2b. As in Fig. 2a except for IR in winter (DJF) at 15°N, 180°.

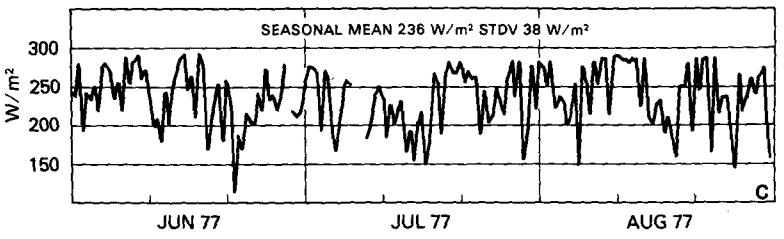

FIG. 2c. As in Fig. 2a except for outgoing IR in summer (JJA) at 7.5°N, 150°E.

In performing such a space-time analysis one must check that the correlations are not affected by the variations in viewing angle or local time associated with the observing system of the polar orbiting satellites. In the visible channel, for example, we have found spatial correlation patterns aligned with the satellite orbit tracks. Such effects are associated with the non-Lambertian angular dependence of the shortwave reflectivity of clouds, and are clearly visible in the composited imagery (Environmental Satellite Imagery, NOAA). Such measurement-related correlations are not found in the IR. The local time variation of $\sim \pm 1$ h across a given orbit track is evident in the IR over Australia where there is a strong diurnal cycle in surface temperature. However, in the next section we show that the diurnal cycle does not appear in IR lag correlations over the Pacific. The real time difference of ~ 2 h between adjacent orbit tracks may cause some eastward moving cloud systems to be missed or westward moving ones to be observed twice. With a typical 10 m s^{-1} advection speed, the correlation patterns discussed in Section 4 would move only a small fraction of their diameter in 2 h, so that any error in the characteristic scales would be small. Finally, the first and last orbit tracks on a given day (midnight to midnight GMT) have a real time difference of ~ 24 h. The boundary of the first and last tracks crossing the equator at 0900 or 2100 LT is near 45°W or 135°E, respectively. If the points p_1 or p_2 in (1) are chosen on opposite sides of such a boundary, some care is needed to determine the correct time lag in the data.

3. Eulerian correlation times

In this section we first examine the IR signals at four 2½° × 2½° gridpoints which are representative of four different regimes in total outgoing IR over the Pacific Ocean. We then review some features of the contour maps of winter and summer IR mean values and standard deviations over the Pacific. These have been previously discussed by a number of authors, most recently Hartmann and Short (1980), Murakami (1980a) and Heddinghaus and Kreuger (1981). We then study the time-lagged autocorrelation functions at the four representative gridpoints. Then variations of the characteristic times over the Pacific are shown in contours of the 1-day lag autocorrelations. These share some of the features of the standard deviation maps, and show an even clearer signature of the midlatitude storm tracks. Finally we study the changes in the autocorrelation functions in the four IR regimes as the 2½° × 2½° averaging area is increased.

Single-season time series of total outgoing IR at four representative 2½° × 2½° gridpoints are shown in Fig. 2, along with mean values and standard deviations (σ) for the season shown. Gaps indicate missing data. Note that no detectable seasonal trends are evident. A convenient rule of thumb relating effective radiative temperature T to derived IR values is given by the linear correlation [see Gruber and Winston (1978) and references therein]

$$\Delta \mathrm{IR}/\Delta T \approx 2\mathrm{W\ m^{-2}\ (°C)^{-1}}, \tag{2}$$

with the intercept

$$\mathrm{IR} \approx 250\ \mathrm{W\ m^{-2}\ at}\ T = 0°\mathrm{C}. \tag{3}$$

Fig. 2a shows the signal on the dateline at 40°N, obtained in the presence of highly variable wintertime cloudiness associated with the midlatitude storm track. Note that none of the values exceed the mean by 2σ (52 W m^{-2}), while quite a few fall below

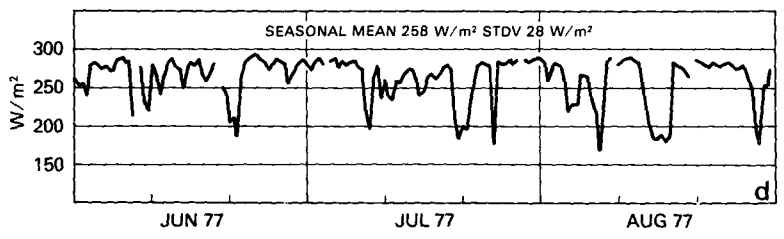

FIG. 2d. As in Fig. 2a except for outgoing IR in summer (JJA) at 20°S, 165°E.

it by that amount. The frequency distribution for all four winters in this region, shown at the upper left, has a long tail of values down to about 140 W m^{-2}. For increasing IR the distribution rises to a peak near one standard deviation above the mean, then abruptly drops to zero at 270 W m^{-2}. According to (2) and (3) the upper cutoff corresponds to $T \approx 10°C$, typical of the mid-Pacific Ocean surface in winter. The lower extreme of 140 W m^{-2} corresponds to $T \approx -55°C$ which occurs about 10 km above the surface for a 6½°C km^{-1} lapse rate. The product of the distribution times the squared deviations from the mean is at the upper right. It vanishes at the mean by definition, has a broad peak at low IR values characteristic of 8 km heights, and a small secondary peak at high values characteristic of 1½ km boundary layer heights. The integral of this product, namely the variance, is dominated by the low IR deviations associated with high cloudiness, which in the storm track constitute ~70% of the variance.

By contrast, the signal at 15°N in the central Pacific, shown in Fig. 2b for the same season as in 2a, shows characteristics typical of a subtropical dry zone. Periods of persistently high values which tend to remain within 1σ (10 W m^{-2}) of the mean are interrupted by brief bursts of values 4σ below the mean. Here the upper cutoff of 300 W m^{-2} corresponds to surface temperatures near 25°C. Clouds cause sudden decreases of 40 W m^{-2} or more (100 W m^{-2} in other years at the same point) but the relative scarcity of such events in this region greatly reduces their impact on means and variances. Diurnal variations of 10 W m^{-2} can be seen at times, but most of the variance here is from clouds which are low or cover only a small fraction of the 2½° area.

Fig. 2c shows the signal at 7.5°N in the summer, with characteristics typical of the ITCZ. The highest values here, approaching 300 W m^{-2}, resemble those in the 15°N wintertime dry zone, while the lowest values, frequently down to 150 W m^{-2}, correspond to temperatures colder than typical cloud top values in the midlatitude storm track. With a tropical lapse rate of 5.5°C km^{-1} such a 75°C drop in effective temperature corresponds to ~13.5 km cloud-top heights.

Fig. 2d shows the IR signal in the southwest tropical Pacific during summer. The upper cutoff here is similar to that in 2b and 2c, since the horizontal temperature gradient of the tropical ocean is small. The variance, however, is closer to that in 2a, the midlatitude storm track. While the similar variance makes the time series shown in 2d appear somewhat similar to that in 2a, we shall see that it is quite distinct in its temporal and spatial character.

Fig. 3a shows the contours of mean outgoing IR in winter obtained by averaging the signal over the four 90-day winters at each gridpoint. Values less than 240 W m^{-2} are shaded. These occur poleward of 30°N and 45°S, where the decrease is correlated with the decreasing surface temperatures and increasing cloudiness, and also in the western Pacific in the 5°N–15°S zone, where the effective radiative temperature is reduced by the high frequency of upper level clouds. Values > 280 W m^{-2} are stippled, and occur in relatively cloud-free zones over the Australian deserts and the north central Pacific, and over the cold water current regime of the southeast tropical Pacific where low clouds dominate. The locations of the two winter signals of Figs. 2a and 2b are indicated here and in later figures by the letters **a** and **b**.

The summer IR mean values are given in Fig. 3b, with the letters **c** and **d** locating the time series of Figs. 2c and 2d. Seasonal changes from winter to summer are apparent. The northern continents are now relatively warmer. The gradient across the Antarctic continental edge is sharper. The ITCZ north of the equator is more prominent, while northern Australia is relatively cloud-free during its dry season.

Contours of standard deviations for winter and summer are shown in Figs. 4a and 4b, respectively, with the four gridpoints of Fig. 2 again indicated by letter on the appropriate seasonal map. As in Fig. 2 the 0900 and 2100 LT variances were computed separately and then averaged. This reduces the variance significantly over Australia but has little effect over the Pacific. Note that the single season standard deviations in Fig. 2 differ somewhat from the four-season average standard deviations at **a**–**d** in Fig. 4 due to interannual variability. While such slow variations are certainly of interest (see, e.g., Heddinghaus and Krueger, 1981), we note that the qualitative features of the contours in Fig. 4 are remarkably stable from year to year.

The latitudinal decrease in variance poleward of ~50° in both hemispheres reflects the decrease in cloud-to-ground temperature differences due to decreased surface temperature and tropopause height. This also contributes to the enhancement of variance over the warmer northern continents in summer. Values of σ less than 20 W m^{-2} are shaded and those greater than 40 W m^{-2} are stippled. The low variance shaded regions within 30° of the equator are clearly associated with the stippled subsidence zones in the mean maps. The high-variance regions on the other hand are clearly associated with the low mean ITCZ, the variance maxima in the tropical western Pacific being enhanced north of the equator during summer and south of the equator during winter. These maxima correspond closely with the shaded minimum IR regions on the mean maps. Some indication of the storm tracks is shown by the relatively high variance areas occurring between the low-variance subtropics and polar regions.

It should already be clear from Figs. 3 and 4 that

the points a, b, c and d are representative of four distinct Pacific cloudiness regimes, each of which extends over many gridpoints surrounding the chosen four. We now examine the characteristic times at these chosen points, and show that they are also representative of each regime.

The solid lines in Figs. 5a–5d represent the time-lagged autocorrelation functions $\rho(\tau)$[$p_1 = p_2$ in Eq. (1)] for the same four gridpoints as in previous figures. The IR time series at each point are lagged in 12 h multiples, and the resulting correlation is averaged over the four available seasons. We ignore the dashed lines for the present. The most striking feature here is the rapid decrease of correlation with increased lag. In the storm track (a) the correlation drops to zero in ~12 h, reaches a negative minimum

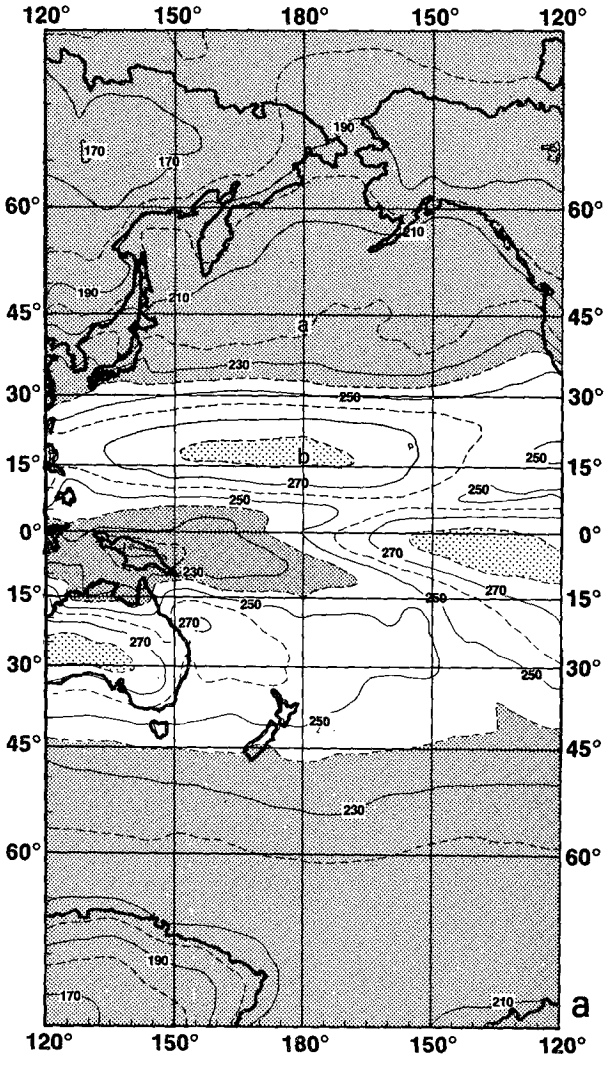

FIG. 3a. Mean outgoing IR for the winter seasons (DJF) of 1975–78 on a Mercator projection. Contour interval is every 10 W m^{-2} with values > 280 W m^{-2} stippled and values < 240 W m^{-2} shaded.

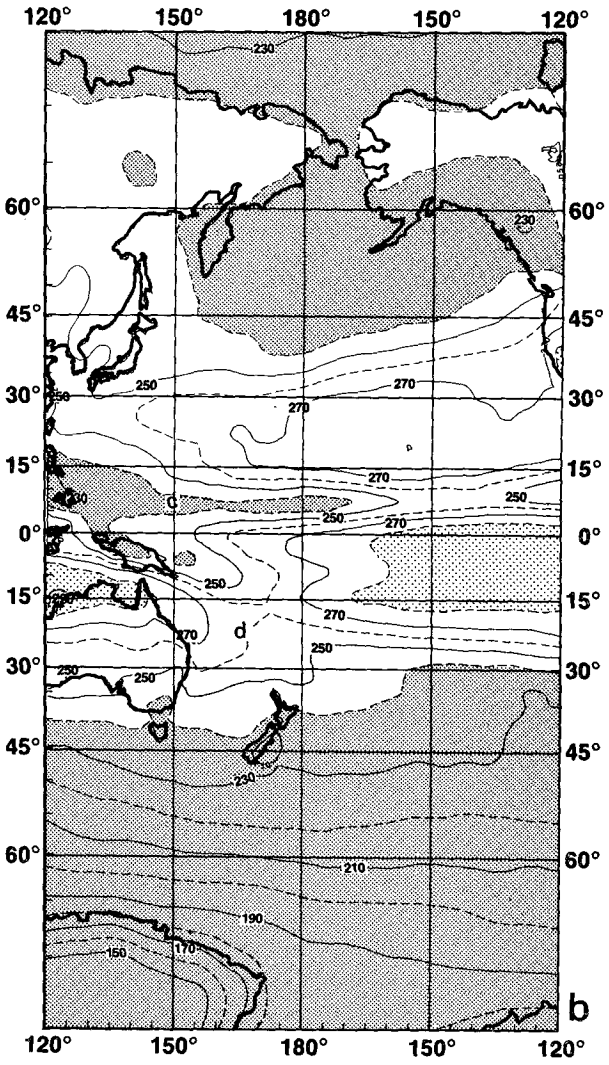

FIG. 3b. As in Fig. 3a, but for the summer seasons (June, July, Aug.) of 1974–77.

at one day, and returns to near zero at three days and beyond. Similarly, in the subsidence zone (b) and the ITCZ (c), while the correlations decrease more slowly, they are all near zero for lags of three days or more.

Precise error estimates for $\rho(\tau)$ unfortunately involve unknown fourth-moment statistics, but if we take three days as an effective time between independent estimates we expect sampling fluctuations in $\rho(\tau)$ at large τ on the order of $(4 \times 90/3)^{-1/2} = 0.09$. This is not significantly exceeded out to lags of about twice those shown in a–c. For lags $\gtrsim$10% of the total record length ρ ceases to be well determined due to insufficient overlap between the series and its lagged counterpart.

The correlation in the southwest tropical Pacific (d) has been plotted on a scale which includes longer

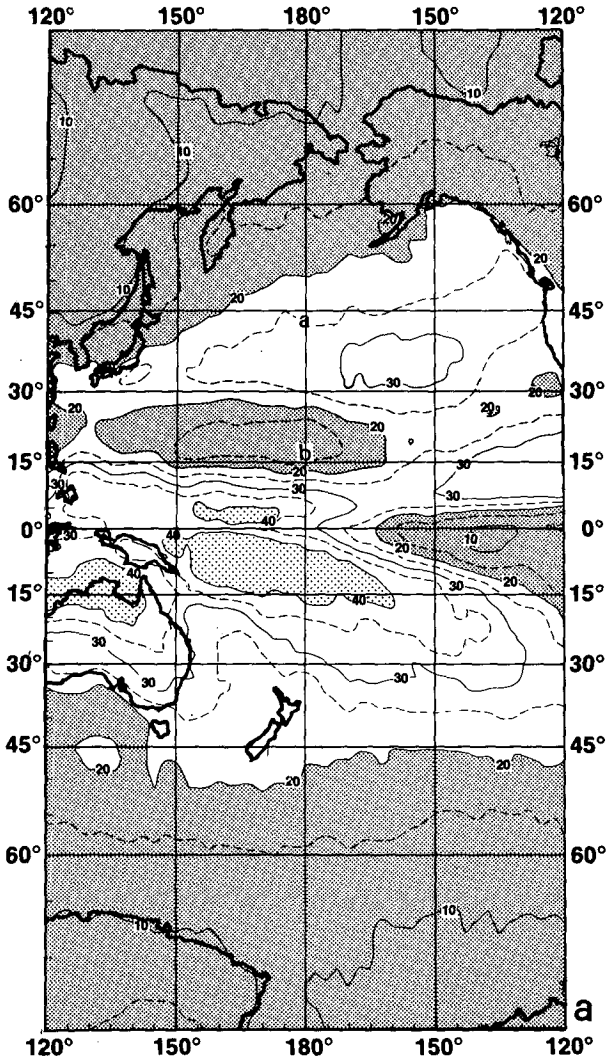

FIG. 4a. Four-season average of the standard deviation of outgoing IR for winter (DJF) computed from day-to-day and night-to-night variations. Contour interval is every 5 W m^{-2} with values > 40 W m^{-2} stippled and values < 20 W m^{-2} shaded.

lags. It shows a distinctive negative correlation which peaks at a 5-day lag and then returns to zero. We shall see that the behavior in this region represents an upper limit of IR correlation lengths and times in the Pacific.

A feature to note at all four locations is the absence of any visible diurnal cycle. It evidently has insufficient variance compared with nonperiodic fluctuations to be detectable in mid oceanic IR correlations (though it may be detectable as a small spike in the spectra). By contrast, there is a clear 24 h period in $\rho(\tau)$ over Australia (not shown). Its amplitude relative to the nonperiodic part increases with averaging area.

Figs. 6a and 6b show contours of IR correlations at lag τ = 1 day over the Pacific in winter and summer, respectively. Covariances between successive mornings and successive evenings were computed separately and then averaged, so that diurnal effects are eliminated in the same way as for the standard deviations in Fig. 4. This again has little effect over the ocean, as expected from the lack of 24 h periodicities in Fig. 5. The contour interval in Fig. 6 is 0.1, with values less than 0.1 shaded and those greater than 0.3 stippled. As in Fig. 5 the most striking feature is again the apparent lack of day-to-day persistence even in regions of subsidence. Corresponding e-folding times $[-1/\ln\rho(1)]$ are less than 2 days everywhere in both seasons. The winter contours appear remarkably zonal, with small or negative lag 1 correlations in the northern and southern midlatitude storm tracks, and larger values (more persistence) between 30°N and 30°S, interrupted by a minimum centered at ~5°N. The summer contours

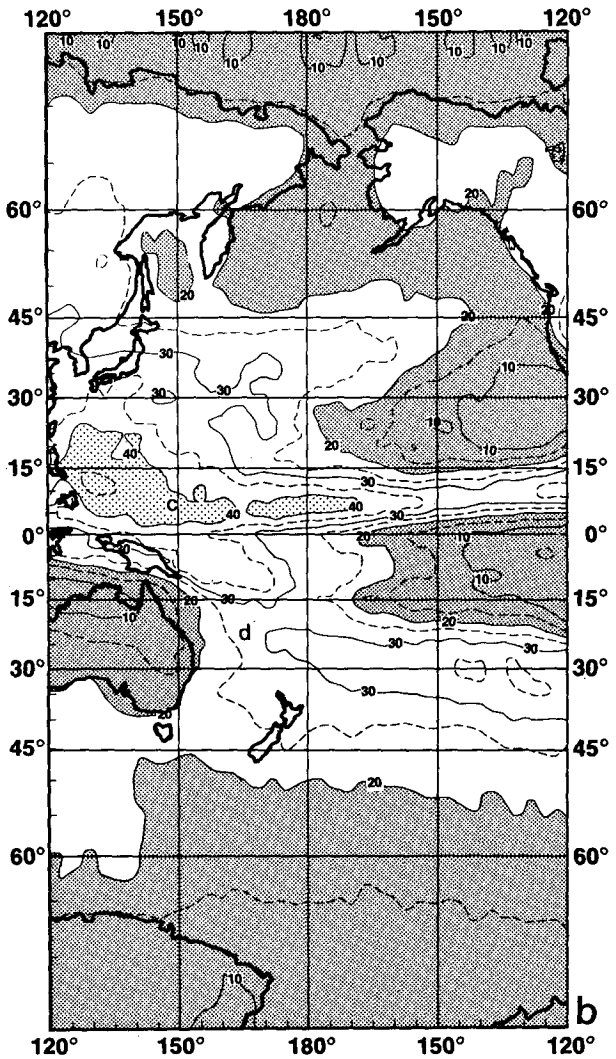

FIG. 4b. As in Fig. 4a, but for the summer seasons (JJA).

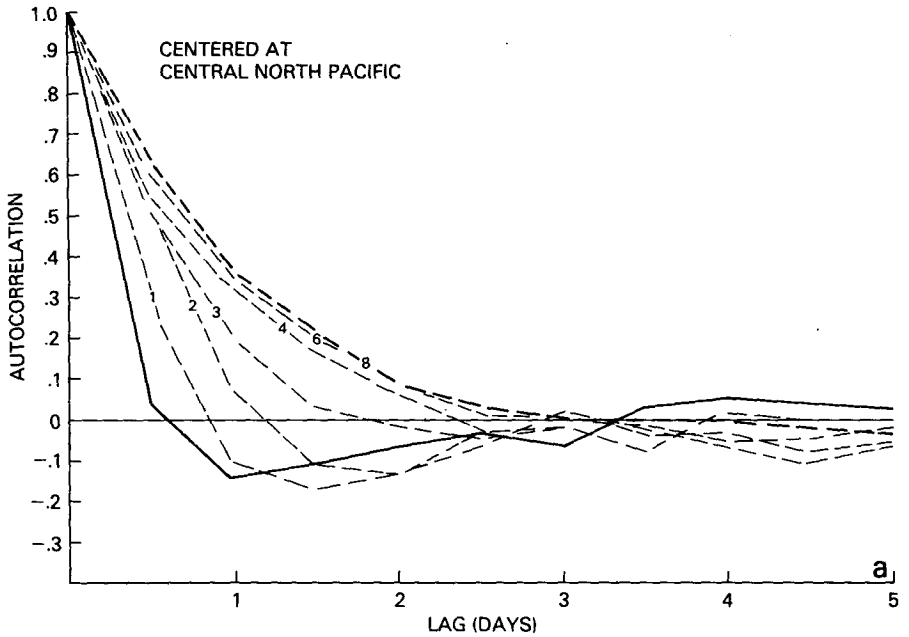

FIG. 5a. Autocorrelation function for the North Pacific signal, part of which is shown in Fig. 2a. Solid line is for the single gridpoint. Dashed lines are for areal multiples of the zero-lag correlation diameter (discussed in Section 4 of the text) extended in an east-west direction. The north-south extent of the averaging areas is one correlation diameter, centered on the gridpoint at 40°N, 180° during winter (DJF).

are more complex. Compared to winter, there appears to be more persistence in midlatitudes in both hemispheres. For example, $\rho(1)$ now exceeds 0.2 south of New Zealand, and regions of negative $\rho(1)$ cover a much smaller area. On the other hand, values of $\rho(1)$ within 30° of the equator are generally smaller in summer in both hemispheres, falling below 0.1 in the 5°N minimum. Summer values are also smaller poleward of 60°N.

Although e-folding times are less than 2 days for

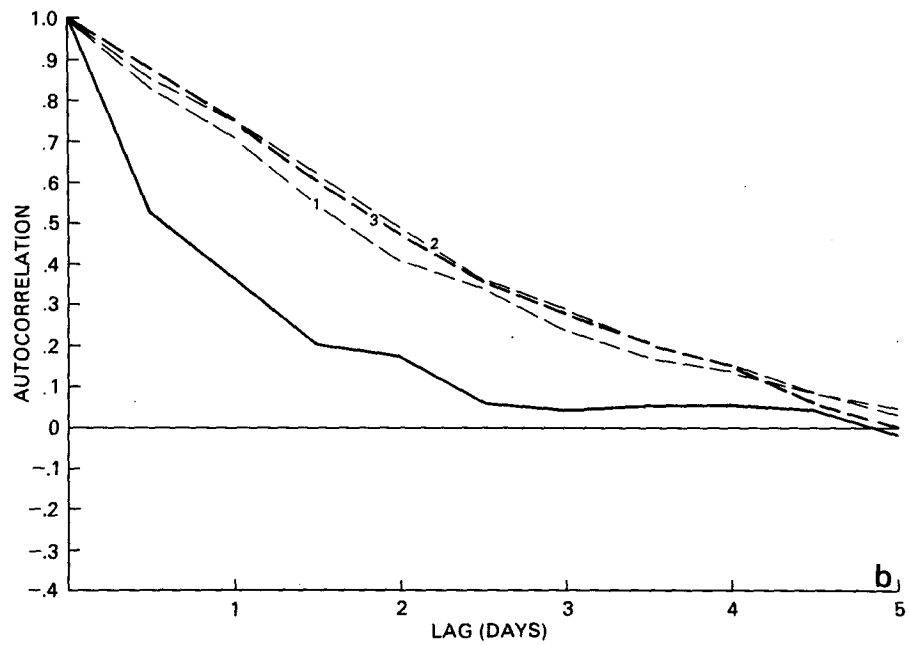

FIG. 5b. As in Fig. 5a, but centered on the gridpoint at 15°N, 180° during winter (DJF).

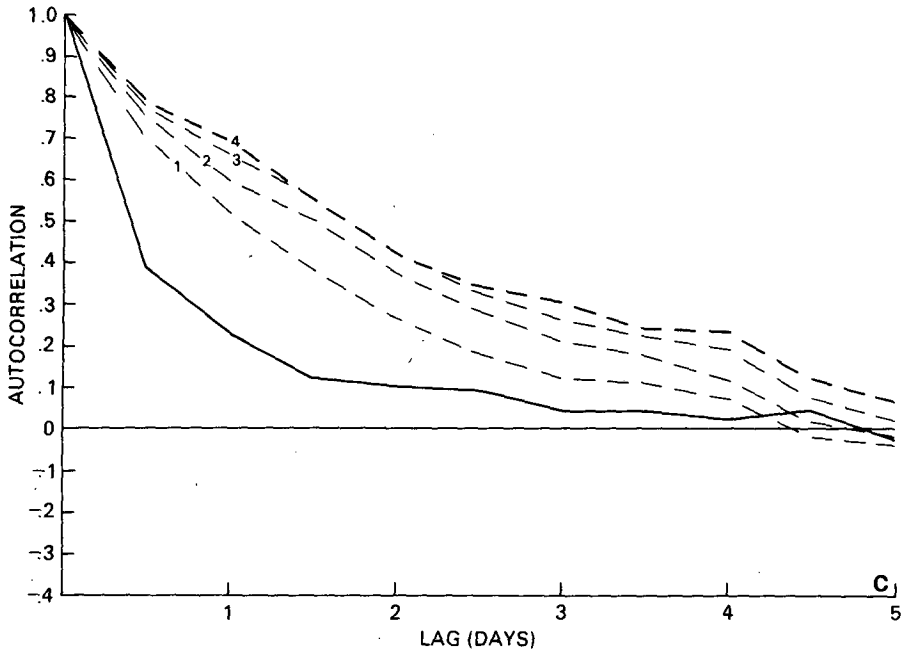

FIG. 5c. As in Fig. 5a, but centered on the gridpoint at 7.5°N, 165°E during summer (JJA).

the individual gridpoints in Fig. 6, rather than representing short cloudiness time scales, these times might instead reflect the advection of short length scale cloudiness past the gridpoint. Assume, for example, that the Lagrangian time scales of cloudiness are much longer than 2 days. Then a single 2½° gridpoint takes a "snapshot" of a slightly shifted portion of the cloudiness each day due to advection, and the resulting signal is correlated only over the time it takes to advect one correlation length. At 10 m s^{-1}, for example, the advection would be 16° in 2 days at the equator, which is six gridpoints or 1728 km. This is a good estimate of correlation lengths in the subtropics, as we shall see in the next section; however, the assumption of long intrinsic time scales is not correct, as we shall now see.

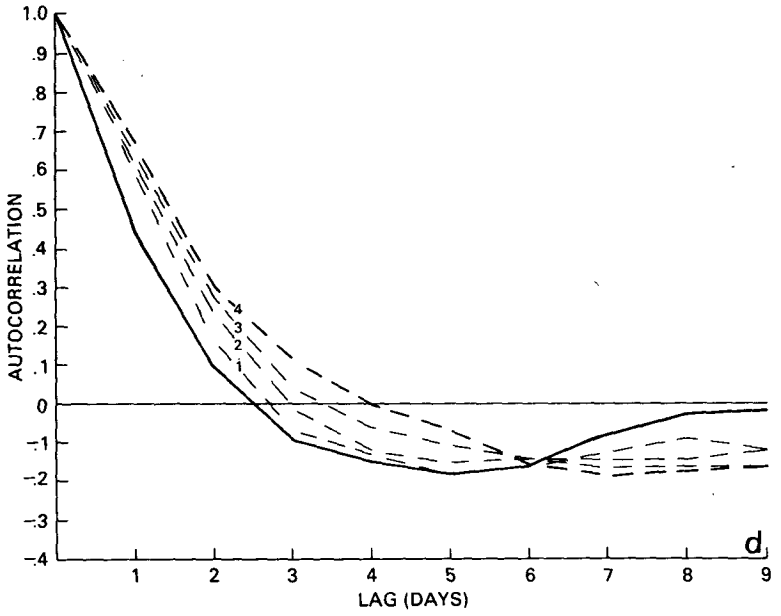

FIG. 5d. As in Fig. 5a, but centered on the gridpoint at 20°S, 165°E during summer (JJA).

In the Appendix a simple model is used to motivate the idea that advection effects may be eliminated by averaging the signal over successively larger areas. As the area becomes large compared to typical advection lengths, the correlation time of the averaged signal approaches the Lagrangian time of the systems within the region. This result is verified empirically in the following section. It implies that if cloudiness were highly persistent it would produce a highly persistent regional signal even though gridpoint signals may be highly transitory due to advection. We now show that in fact the regionally averaged IR, while more persistent than gridpoint IR, is still highly transitory.

The dashed lines in Fig. 5 represent $\rho(\tau)$ for IR signals averaged over one correlation diameter in latitude and various correlation diameters in longitude, as indicated by the labels. (Correlation diameters are given in Fig. 8, and discussed in the next section.) In the storm track the negative $\rho(1)$ shown for the single gridpoint (the solid line in Fig. 5a) becomes positive by the time the area reaches two correlations diameters in longitude. It rises to 0.32 for an area four correlation diameters long, and then appears to be reaching a limit as the area length increases to eight correlation diameters. The limiting curve is nearly exponential, suggesting a first-order Markov model (see appendix). The e-folding time is $\sim$1 day. In the subsidence zone (b) the limit is nearly reached for an area equal to a single correlation diameter. Here $\rho(1)$ exceeds 0.7, which corresponds to an e-folding time >3 days, although ρ actually reaches $1/e$ at $\tau = 2.5$ days. The fact that $\rho(1)$ reaches a limit quickly in the dry zone, while it continues to

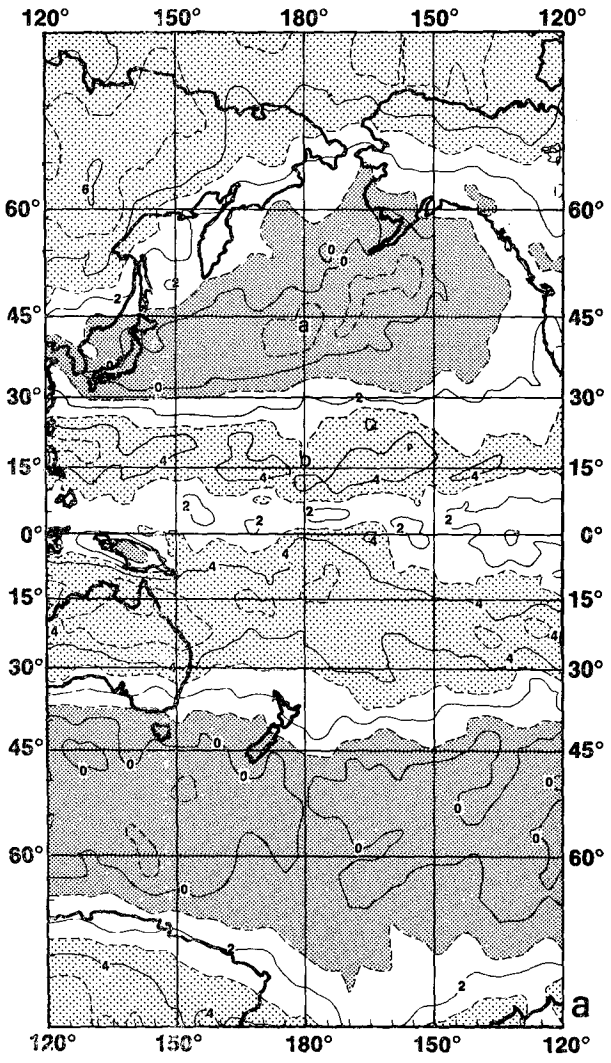

FIG. 6a. Winter (DJF) one-day lag autocorrelation function (×10) computed for the time series at each gridpoint and contoured in map form. Contour interval is every 1 (0.1 × 10) with values > 3 stippled and values < 1 shaded.

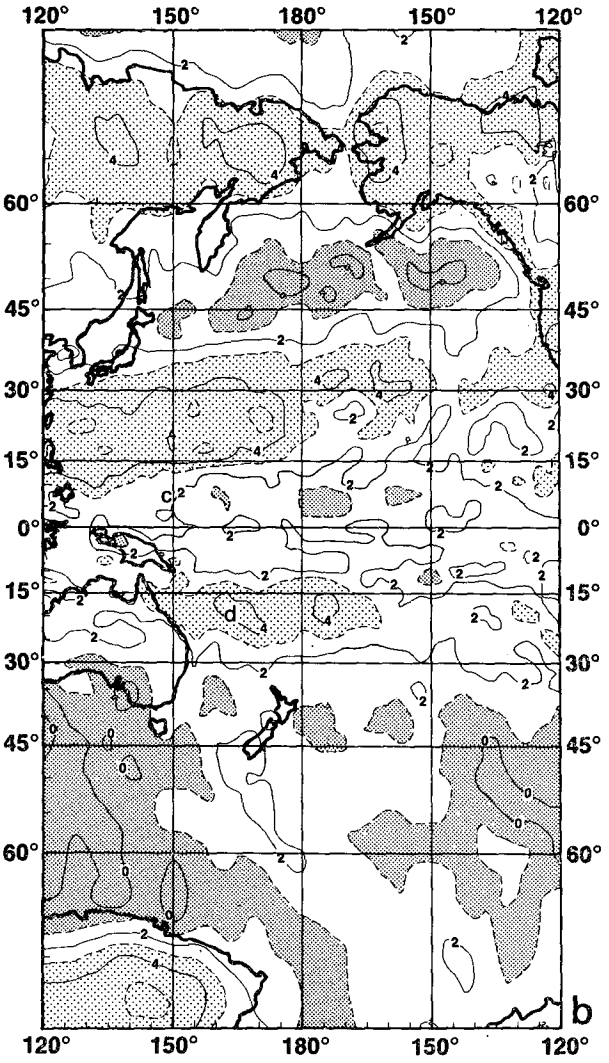

FIG. 6b. As in Fig. 6a, but for summer (JJA).

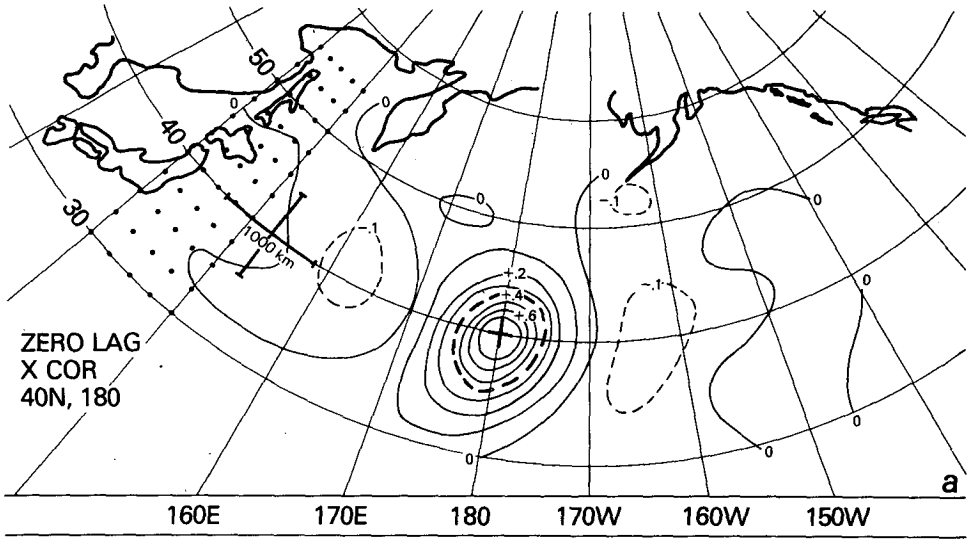

FIG. 7a. Polar stereographic projection contour map of zero-lag cross correlation between the signal at 40°N, 180° and other gridpoints for the winter season. Heavy dots indicate the gridpoint spacing. Contour interval is every 0.1 with the zero-lag correlation diameter approximated by the heavy dashed 0.4 contour.

change in the storm track as the area increases by a factor of 4, implies that the advection length is only a fraction of the correlation diameter in the dry zone, but perhaps two or three correlation diameters in midlatitudes. This will be verified directly in the next section.

In the ITCZ (c) the limit is approached as in the storm track, but the resulting time scale resembles that in the dry zone. The advection in this region is easterly, as shown in the next section.

Finally, in the southwest tropical Pacific (d) the limiting behavior of $\rho(1)$ is much like that at (a) or (c), but the negative correlation (at $\tau = 5$ days for the single gridpoint) is not eliminated by area averaging as it is in the storm track, but instead tends to persist to longer lag times. In the next section we show that the correlations in this region are associated with large spatial scales, the positive correlations advecting southeastward with origins as distant as 2500 km to the northwest. Elsewhere, however, cloudiness advection lengths and corresponding Lagrangian lifetimes are considerably shorter, as indicated by the 1-day autocorrelation time of the storm-track-averaged IR in Fig. 5a.

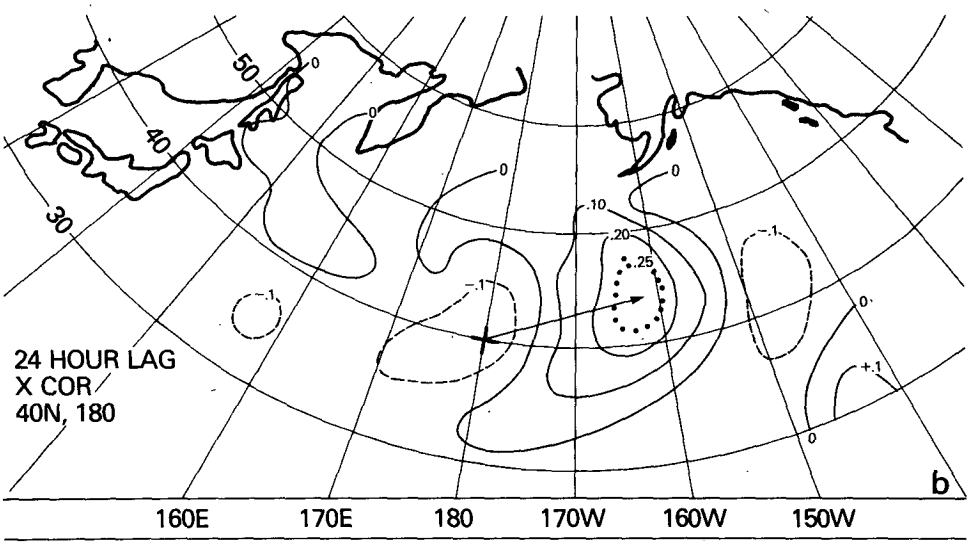

FIG. 7b. Contour map of the cross correlation between the signal at 40°N, 180° and other gridpoints one day later for the winter season (DJF).

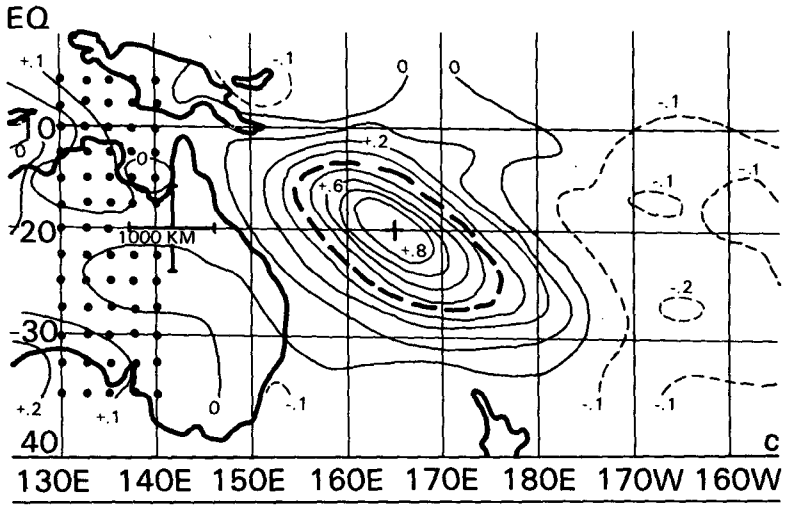

FIG. 7c. As in Fig. 7a, but on a Mercator projection with the central gridpoint at 20°S, 165°E for the summer season (JJA).

4. Lagrangian correlation times

The 1-day lag autocorrelations shown in Fig. 6 can be misleading. For example, the areas near 15°N and 15°S during winter (DJF) appear to be similar—both have autocorrelation times of ~1 day. Yet these are very different circulation regimes. One is the South Pacific Convergence and is highly disturbed, and the other is the subtropical dry zone and is relatively cloud free (cf. Figs. 3a and 4a). The apparent similarity disappears when the statistics take account of mean advection. We shall see that the Lagrangian autocorrelation time is also 1 day at 15°S but is double the Eulerian time at 15°N in agreement with the large area result in Fig. 5b.

In this Section we first study the spatial cross correlations between the winter IR signal in the midlatitude storm track (a) and simultaneous and 1-day lagged signals at all other points. Correlations with simultaneous signals determine the correlation length at (a), while correlations with time-lagged signals determine the Lagrangian times and advection lengths. Next these spatial cross correlation characteristics are studied for the summer IR signal in the southwest tropical Pacific (d). Finally, the characteristic scales for all reference points on a 5° × 10° grid over the Pacific are presented in summary form.

Fig. 7a shows contours of equal correlation between the signal at p_1 = (40°N, 180°) ≡ a and simultaneous signals over the Pacific between 30 and

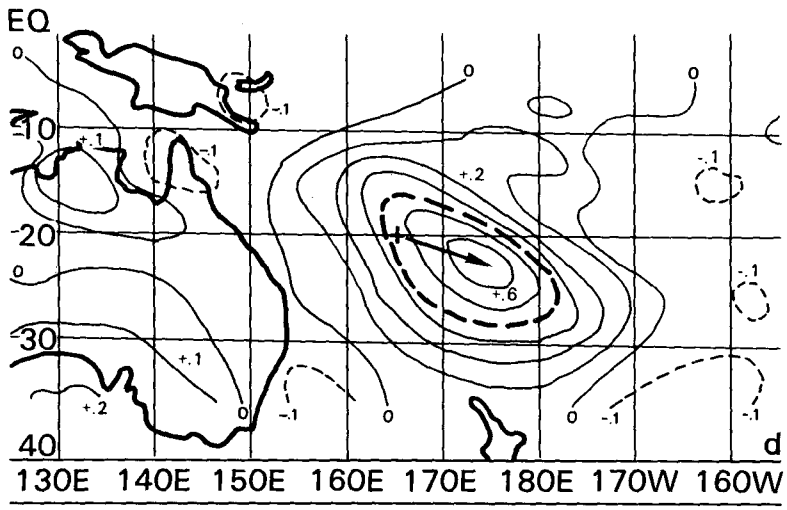

FIG. 7d. As in Fig. 7b, but on a Mercator projection with the central gridpoint at 20°S, 165°E for the summer season (JJA).

55°N; that is, $\rho(\mathbf{a}, \mathbf{p}_2; 0)$ in the notation of Eq. (1). The contour interval is 0.1, the 2½° grid is shown on the left; and at 40°N, 1000 km = 11.8° of longitude. The most obvious feature here is the rapid decorrelation in the vicinity of **a** (indicated by the cross), with ρ decreasing to $1/e$ (0.4, the heavy dashed contour) in about two grid spacings or 500 km. The contours are approximately circular in the vicinity of **a**, consistent with the notion of local statistical isotropy.[1] Negative correlations exceeding −0.1 occur ~18° of longitude to either side of **a**. The 36° wavelength corresponds to wavenumber 10. Elsewhere the correlations fluctuate about zero within ±0.1, the approximate noise level, which may be estimated by a similar sampling argument as for $\rho(\tau)$. The deviations from isotropy near **a** may also be due to the limited sample, so that in the positive correlation region we may assume

$$\rho(\mathbf{a}, \mathbf{p}_2; 0) \approx \rho(r; 0). \tag{4}$$

That is, ρ is a function only of great circle distance $r = |\mathbf{r}|$ within about 1000 km of **a**. This function also remains quite similar as the reference point is moved from **a** to other points in the storm track region, so that in this region the correlations are statistically homogeneous. Fluctuations of geopotential height also tend to be statistically isotropic and homogeneous in midlatitudes (Bertoni and Lund, 1963) with correlations falling to $1/e$ in ~1500 km and negative correlations more than twice those in the IR. Anisotropy is greater at lower latitudes in the IR correlations, as we shall see.

Fig. 7b also shows equal correlation contours with the signal at **a**, but the signals elsewhere are now given a lag time of 1 day; this is $\rho(\mathbf{a}, \mathbf{p}_2; 1)$ in the notation of Eq. (1). The value at $\mathbf{p}_2 = \mathbf{a}$ (the cross) is precisely the lag 1 autocorrelation at the negative minimum of the solid curve in Fig. 5a. However, the spatial correlation pattern shown in Fig. 7b is still dominated by positive values just as in 7a, but the maximum has decreased from 1 to slightly less than $1/e$, and does not occur at $\mathbf{p}_2 = \mathbf{a}$ but rather ~18° to the east. The advection velocity corresponding to an 18° shift per day is

$$|\mathbf{v}| \approx 20 \text{ m s}^{-1}. \tag{5}$$

The wavenumber 10 negative features in 7a also appear shifted in 7b, so that the negative correlation minimum at **a** appears to be merely an artifact of advection rather than any feature of cloudiness evolution at **a**. This explains its absence in the area average lag correlation.

If the signal at **a** is correlated with signals elsewhere having a *lead* time of 1 day, that is $\rho(\mathbf{a}, \mathbf{p}_2; -1)$, the contours appear similar to those in 7b but now shifted ~18° to the *west* of those in 7a. The value at $\mathbf{p}_2 = \mathbf{a}$ is still the same, since $\rho(-\tau) = \rho(\tau)$, but it lies within the eastern negative contour, rather than the western one as in 7b. This symmetry in τ is consistent with the advection of isotropic correlations which are statistically homogeneous. The homogeneity implies that

$$\rho(\mathbf{r}; -\tau) = \rho(-\mathbf{r}; \tau). \tag{6}$$

If the positive lag function on the right-hand-side of Fig. 6 has a peak value at $\mathbf{r} = \mathbf{v}\tau$ (as in Fig. 7b) then the negative lag function has the same peak value at $\mathbf{r} = -\mathbf{v}\tau$.

We have not shown the correlation patterns at $\mathbf{p}_1 = (15°\text{N}, 180°) = \mathbf{b}$ and $\mathbf{p}_1 = (7.5°\text{N}, 150°\text{E}) = \mathbf{c}$; these are qualitatively similar to those at **a**, with some quantitative differences: At **b**, the zero-lag correlation diameter increases from the 1000 km diameter seen in midlatitudes to ~1700 km, and no significant negatives appear. At 1-day lag the reference point at **b** is still within the $1/e$ contour and the maximum is only slightly shifted. At **c**, in the ITCZ in summer, the correlation length is about 1200 km and the advection of the positive correlation peak is toward the west-northwest at ~6° day^{-1} or 8 m s^{-1}. These characteristic scales in the ITCZ are consistent with those determined in previous studies of westward propagating cloud clusters in the tropical Pacific (e.g., Chang, 1970; Williams and Gray, 1973). Another difference between the correlation patterns at **b** and **c** compared to those at **a** is increased anisotropy. For a clearer case of this we turn to the southwest tropical Pacific.

Figs. 7c and 7d show the zero lag and 1-day lag correlation patterns at $\mathbf{p}_1 = (20°\text{S}, 165°\text{E}) = \mathbf{d}$ in NH summer. Here we see longer length scales and a greater degree of anisotropy than at 40 N. The zero lag $1/e$ contour is about 2400 km across in the southeast direction, and about half as wide. This elongation of the zero lag positive correlation is nearly aligned with the shift of the 1-day lag maximum, which is about $1/\sqrt{e}$ and occurs ~7.5° southeast of **d**, corresponding to 10 m s^{-1} advection. The 2-day lag maximum (not shown) is about $1/e$ and occurs further southeast near the dateline. In approximate agreement with (6), similar maximum values occur to the northwest for 1- and 2-day lead times (not shown), the latter being about $1/e$ and occurring near 150°E. Unlike what happens at 40°N, negative spatial correlations corresponding to the minimum autocorrelation at lag 5 days in Fig. 5d do not appear in the lag zero or 1-day spatial patterns of Figs. 7c and 7d, but only develop at larger lags. Thus advection of negative spatial correlations, which produces the negative autocorrelation in mid-

[1] The stereographic projection in Figs. 7a and 7b has the property of mapping an arbitrary circle on the sphere into a circle on the projection plane, and it is therefore ideal for testing isotropy. However, IR correlation lengths are small enough that a Mercator projection creates little anisotropy.

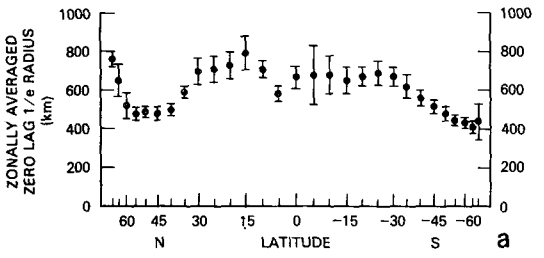

FIG. 8a. Latitudinal cross section of the zonally averaged zero-lag correlation radii for winter (DJF). Error bars are standard deviations for the longitude interval which has been analyzed.

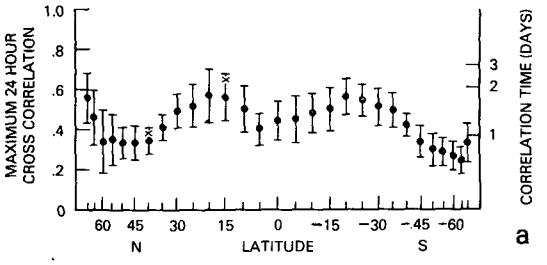

FIG. 9a. As in Fig. 8a, but for the maximum one-day cross correlation.

latitudes, appears to play little role in producing the negative autocorrelation in the southwest tropical Pacific. Lag autocorrelations of large-area-averaged IR, not being strongly affected by advection (see Appendix), are therefore positive in midlatitudes but negative here.

We have computed zero and 1-day lag spatial patterns for reference points every 5° of latitude and every 10° of longitude from 140°E to 140°W. The results are summarized in Figs. 8–10. An average correlation length at each point is determined by counting the number of 2½° areas falling within the zero lag $1/e$ contour, and computing the diameter of a circle having this same area. We then compute the mean and standard deviation of the nine correlation diameters at each latitude. The result is given in Fig. 8, where the $1/e$ correlation radius (half the correlation diameter) is plotted as a dot at each latitude, with error bars one standard deviation above and below the mean. Note that in winter (Fig. 8a) the correlation radius has a latitude dependence similar to that of $\rho(1)$ (see Fig. 6a). At latitudes having less cloudiness, as at 15 N to 30 N, IR fluctuations are larger scale and there is more persistence at individual points. Where there is more cloudiness, as at 40–60°N, IR fluctuations are smaller scale and less persistent. However, the Eulerian times are not determined by length scales alone, but variations in advection also play a role, especially in seasonal changes. In summer (Fig. 8b) the correlation radius at 5°N is the same as in winter while from 5–15°S and from 15–30°N it has decreased. The corresponding $\rho(1)$ in Fig. 6b has also decreased from 5–15°S but not from 15–30°N. This is due to the fact that advection has decreased in the northern zone, but increased in the southern zone, as we shall see. Note that at 20°S the zonal mean correlation radius is slightly larger in summer. The error bars are also larger because larger scales do not occur over the whole zone, but only in the western region around d. We shall see that advection has actually increased here, but this is offset by the larger scales, so that $\rho(1)$ remains about the same.

The Lagrangian correlation time can be expressed as $-1/\ln(\rho_{max})$ where ρ_{max} is the maximum lag 1-day cross correlation. The value of ρ_{max} was determined for each of the nine reference points at each latitude for each of the four winters and summers. The mean and standard deviation of the 36 values at each latitude in winter and summer is given in Fig. 9. The left-hand scale gives the maximum correlation, and the right hand scale the Lagrangian correlation time. The latitude dependence of ρ_{max} is similar to that of the correlation radius, so that the direct relation between persistence and length scale is not purely an artifact of advection. The $1/e$ autocorrelation times of the regional averages determined from Figs. 5a–5d are indicated by the four crosses in Fig. 9. The Lagrangian times agree with the characteristic times of the regional averages in the midlatitudes and subtropics but not in the ITCZ (c) where the Lagrangian time is a minimum but the characteristic time of the area-averaged IR is a maximum. The minimum Lagrangian time suggests the influence of smaller spatial scales in the ITCZ (see for example Hayden, 1970). In fact the ITCZ minima in both

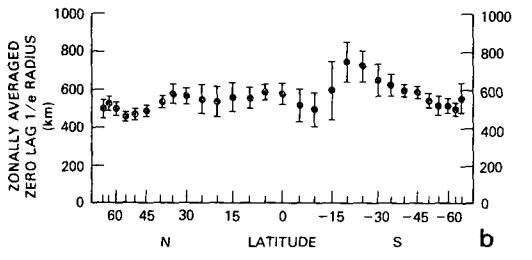

FIG. 8b. As in Fig. 8a, but for summer (JJA).

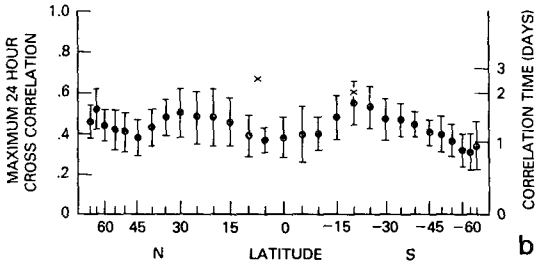

FIG. 9b. As in Fig. 9a, but for the summer season (JJA).

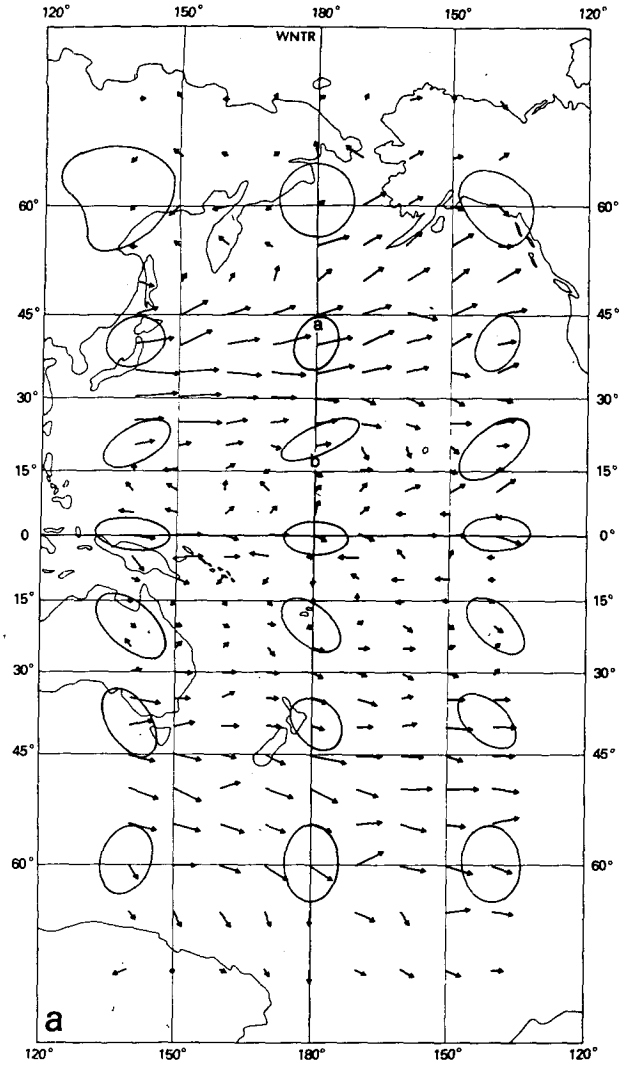

FIG. 10a. Winter season (DJF) vectors indicating the direction and displacement of the 1-day lag correlation between the grid point at the tail of the vector and other gridpoints. The vector length is proportional to the velocity associated with the 1-day displacement, with a vector length of 10° of longitude equaling a velocity of 20 m s^{-1}. Also included is a sampling of the $1/e$ zero-lag correlation contours similar to those in Figs. 7a and 7c.

Figs. 8 and 9 might be further reduced with higher resolution. At the same time the relative persistence of area-averaged IR over the ITCZ suggests the importance of larger scales as well. Perhaps our most basic result, however, is that even in the regions having the largest spatial scales, characteristic times are limited to ~ three days.

Finally, arrows such as those shown in Figs. 7b and 7d, originating at the reference point and directed toward the location of the maximum lag 1-day correlation, are shown on the 5° × 10° grid in Fig. 10. For a 20° × 40° subset the zero lag $1/e$ correlation contours are also shown, and are discussed at the end of this section. The arrow lengths have been scaled so that 10° of longitude represents 20 m s^{-1}. The associated advection lengths may be obtained by multiplying by the Lagrangian correlation times. Midlatitude storm tracks are apparent in both hemispheres in Fig. 10a. Their axes are aligned with the negative $\rho(1)$ regions in Fig. 6a. Regions of minimum advection, at 15°N and from 10–30°S, correspond to the maximum $\rho(1)$ regions in Fig. 6a. The difference in advection between the storm track (a) and the subsidence zone (b) explains the different dependence on the averaging area seen in Figs. 5a and 5b. Even with the relatively long 2½-day Lagrangian correlation time at (b), the 5 m s^{-1} advection still gives an advection length only half as long as the correlation length, whereas at a the advection length is twice the correlation length. Curve 4 in Fig. 5a and curve 1 in Fig. 5b therefore both refer to areas about two advection lengths long.

In the summer (Fig. 10b) storm track advection

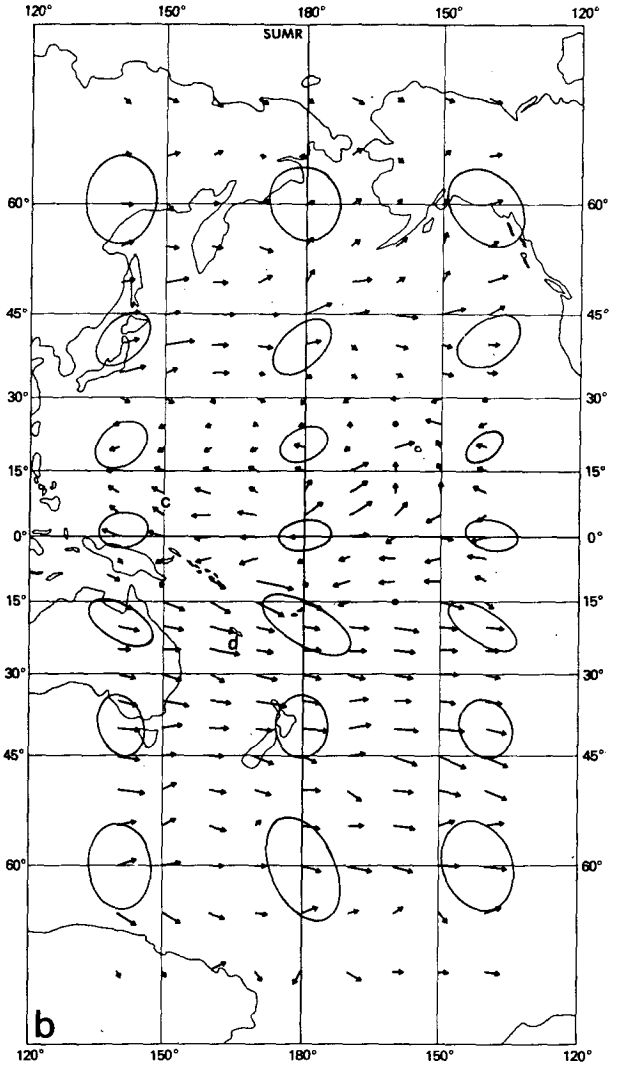

FIG. 10b. As in Fig. 10a, but for the summer season (JJA).

is reduced. Minimum advection now occurs from 15–30°N. From 15–30°S, where minimum advection occurs in NH winter, increased westerly advection occurs in summer. Increased easterly advection occurs from 10°N to 5°S over the western Pacific and from 5–10°S over the eastern Pacific. Reduced advection is associated with regions of increased persistence as seen in Fig. 6b, and increased advection is associated with reduced persistence, except in the southwest Pacific (d) where the large spatial scales seen in Figs. 7c and 7d tend to maintain the persistence in this season despite increased advection.

The correlation arrows in Fig. 10 cannot be simply related to seasonal mean winds at any one pressure level due to their dependence on the vertical motion field and vertical cloudiness distribution. In midlatitudes the arrows correspond to mid-tropospheric winds, consistent with the idea of a steering level, i.e., a level at which the disturbance speed equals the wind speed. In the western tropical North Pacific the arrows more closely match the upper tropospheric winds and are similar to the average speed of the synoptic-scale wave disturbances studied by Reed and Recker (1971). The arrows southeast of Hawaii in Fig. 10b are opposite to the tropical easterly flow at 700 mb in summer, and instead resemble the southwesterly flow in the mid-oceanic trough at 300 mb. In general the locations of the larger arrows correspond with seasonal mean jet stream locations, while the arrow magnitudes in midlatitudes are as much as a factor of 3 less than jet stream speeds. Space-time velocity correlations in wind-tunnel turbulence also advect more slowly than the mean flow (Fisher and Davies, 1964). It is interesting that such disparate dynamical scales can produce qualitatively similar statistics.

A particularly intriguing region where the advection arrows do not correspond to the seasonal mean winds at any level in the troposphere is along the equator during winter. Here we observe an eastward advection regime ($\sim$10 m s^{-1}) which is confined to the equator, extending in longitude over the whole 80° interval shown. In fact, we have observed the same phenomenon over the Indian Ocean (also during winter). This evidence of eastward propagating disturbances in the outgoing IR signal is suggestive of the Kelvin-wave type disturbances noted in studies of satellite measured albedo (Wallace and Chang, 1972; Zangvil, 1975).

The zero lag $1/e$ correlation contours in Fig. 10 have been expanded at higher latitudes by the Mercator projection, counterbalancing the actual size decrease seen in Fig. 8. However, the shapes are accurately preserved (see footnote in discussion of Fig. 7). The most isotropic regions (shown in Fig. 10) are at 40°N in DJF and at 40°S in JJA. In contrast, at 20°N(°S) we find a prominent SW–NE (NW–SE) tilt, reflecting the mean orientation of transient cloud bands in these regions. Along the equator the contours are stretched E–W, particularly during winter in the eastward advection regime, where the N–S symmetry again suggests equatorially trapped Kelvin waves. The maximum tilt and anisotropy at latitudes of 15°–30° in Fig. 10 may be related to the greater latitudinal wind shear and relative frequency of cloud vortex development. A recent modeling study of Webster (1981), for example, finds the major tilt and anisotropy of tropospheric disturbances occurring on the equatorward side of a midlatitude jet stream axis. Streten and Troup (1973) observed cloud vortex development from pre-existing cloud bands more frequently at 20–35°S than at higher latitudes. Further study is needed to establish the statistical significance and strengthen the dynamical interpretation of the correlation arrows and anisotropies.

5. Discussion

The purpose of this study has been to determine the characteristic temporal and spatial scales of day-to-day changes in cloudiness which dominate the variance of outgoing infrared radiation. The main results may be summarized as follows:

1) Eulerian correlation times are very short, generally less than 1½ days over the Pacific Ocean in both summer and winter. Regional variations can be understood in terms of variations in length scales and variations in mean advection.

2) IR correlation radii vary from a minimum of 400–500 km in midlatitudes (about a factor of 3 less than that of the geopotential height) to a maximum of 800–900 km in the subtropics, decreasing to a secondary minimum of $\sim$600 km in the ITCZ at 5°N.

3) IR spatial correlations tend to be advected with speeds comparable to 700 mb flow. The advection is largely zonal and has maxima at the mean locations of the midlatitude jet streams. Eastward advection extending along the equator in winter is suggestive of the influence of atmospheric Kelvin waves on cloudiness fluctuations.

4) The Lagrangian correlation times are always larger than the Eulerian, but rarely more than a factor of 2. Consequently, characteristic times of IR signals averaged over increasing areas of the Pacific Ocean approach upper limits of three days or less.

The relatively short time scale inferred here for synoptic-scale midlatitude cloud systems is consistent with the results of Streten and Troup (1973) who examined daily mosaics of reflected solar radiation in order to characterize the life cycles of extratropical cloud vortices in the Southern Hemisphere. They found that only 50% of cloud systems first observed as "comma clouds", a sign of early vortex development, developed into systems lasting at least two days.

In closing we mention some directions for further research:

1) The same analysis may be carried out on filtered data. For example, high clouds might be isolated for study. Another possibility is to develop the data into spectral form and examine the time scales of selected wavenumbers in space. The sampling problems of such filtered data must be balanced by some advantage in interpretation.

2) While the present study has shown how characteristic scales vary as the averaging area increases from 2½° × 2½°, it is important to extend the study to smaller averaging areas using higher resolution data.

3) Similar methods of analysis may be applied to other climatological data sets. Also of interest is the cross correlation of other meteorological fields with the satellite data utilized here.

Acknowledgments. It is a pleasure to thank T. L. Bell, A. Gruber, J. Mengel and J. M. Wallace for their assistance and encouragement.

APPENDIX

Area Averaging and Persistence

In this Appendix we introduce a simple stochastic model containing randomly created "cloud dots" having a given probability of decay and a given advection speed. Our purpose here is to motivate the empirical result that the autocorrelation time of an area average IR signal approaches the Lagrangian correlation time as the area size increases. While a number of unrealistic assumptions are made to simplify the derivation, the final result holds in more general circumstances.

We imagine that the IR signal at a given gridpoint $\mathbf{p}$ and time t, $s(\mathbf{p}, t)$, consists of two components: a constant mean cloudiness signal s_0 and a variable number of anomolous "dots" per grid-box $n(\mathbf{p}, t)$, each dot representing a positive or negative deviation from the mean and altering the signal by a given amount Δs; that is, $s = s_0 + n\Delta s$. The dot density is assumed to satisfy the continuity equation

$$\frac{\partial n}{\partial t} + \mathbf{v}\cdot\nabla n - D\nabla^2 n = -\frac{n}{\tau_L} + w, \qquad \text{(A1)}$$

Here $\mathbf{v}$, D and τ_L represent a typical advection velocity, diffusion constant, and decay time, respectively, and are taken to be fixed parameters. The source term w is a Gaussian random variable assumed to be white noise in both space and time.

We consider an average of (A1) over some fixed area A. If we assume that transport across the boundaries of A can be neglected, the advection and diffusion terms can be dropped, and we obtain for the average $n_A \equiv A^{-1}\int n dA$ the Langevin equation

$$\frac{dn_A}{dt} = -\frac{n_A}{\tau_L} + w_A,$$

leading to the well-known exponential (red noise) autocorrelation

$$\rho_A(\tau) \equiv \overline{n_A(t)\, n_A(t+\tau)}/\overline{n_A^2} = e^{-\tau/\tau_L}.$$

Under what conditions can the neglect of transport leading to this simple result be justified? Judging from Fig. 5a the area A must be large. For a more quantitative criterion we must determine the transport dependence of ρ_A. Our approach is to first determine the lag cross-covariance of the dot densities at two arbitrary points $\mathbf{p}$ and $\mathbf{p}'$ (the analogue of Figs. 7a and 7b), then average both $\mathbf{p}$ and $\mathbf{p}'$ over the given area A. To simplify we shall give the results explicitly only for $D = 0$, then qualitatively discuss modifications due to diffusion.

To determine the lag cross-covariance of the dot densities at points $\mathbf{p}$ and $\mathbf{p}'$ we first expand both n and w at the two points into Fourier components, solve (A1) for the components of n at the two points, average the product of the two using the white noise assumption for w, then perform the frequency and wavenumber integrals. The final result for the $D = 0$ case is given by

$$\overline{n(\mathbf{p}, t)\, n(\mathbf{p}', t+\tau)} = k e^{-\tau/\tau_L}\delta(\mathbf{r} - \mathbf{v}\tau). \qquad \text{(A2)}$$

Here k is a constant and $\delta(\mathbf{r} - \mathbf{v}\tau)$ is a Dirac delta function which is zero except when $\mathbf{r} = \mathbf{v}\tau$, where $\mathbf{r}$ is the vector from $\mathbf{p}$ to $\mathbf{p}'$. The exponential factor identifies τ_L as the Lagrangian correlation time. If the delta function were correct, all the correlation in Fig. 7b would be concentrated precisely at the tip of the arrow. This unrealistic concentration of correlation in (A2) is a consequence of the zero correlation length of the forcing and the simplified form of the transport. The correlation would clearly become smeared out if $\mathbf{v}$ were allowed to fluctuate. The effect of velocity fluctuations is simulated by the diffusion term in (A1). However, we find that diffusion and a correlation length in the forcing only affect the autocorrelation for relatively limited areas, not the Lagrangian feature of very large areas which we shall now derive for the $D = 0$ case.

The autocorrelation function of an area average may be obtained from the lag cross covariance in (A2) by integrating the coordinates of each of the two points over the chosen area, then normalizing the result by its value at zero lag. The effect of the delta function in (A2) is that the integral is nonzero only over that part of the fixed area which overlaps with a congruent area of cloudiness having its center shifted by $\mathbf{v}\tau$. For example, a rectangular area aligned with $\mathbf{v}$ and having length d has an autocorrelation given by

$$\rho_A(\tau) = \begin{cases} e^{-\tau/\tau_L}[1 - (v\tau/d)], & \tau \leq d/v \\ 0, & \tau > d/v. \end{cases} \qquad \text{(A3)}$$

For area length $d \gg v\tau_L$ we obtain the desired result

$$\rho_d(\tau) \xrightarrow[d \text{ large}]{} e^{-\tau/\tau_L}. \qquad \text{(A4)}$$

This holds also for non-rectangular areas if d is taken to be the diameter measured parallel to $\mathbf{v}$.

As an example of the criterion that the area length must exceed the advection length in order to neglect transport, consider the IR signal in the midlatitude storm track, where we know from Fig. 7b that the advection length is $\sim 20°$. For the 2½° gridpoint, then, we have the opposite limit to that of (A4), and must instead take $d \ll v\tau_L$ in (A3), which then approaches zero except at $\tau = 0$. This white noise is due to the high-frequency fluctuations associated with the passage of cloudiness systems across the boundaries of the 2½°. As it shrinks to a point the Eulerian correlation time in the $D = 0$ model becomes identically zero due to the zero correlation length. A model with nonzero correlation length gives an Eulerian time at a point equaling the time required for a correlated cloudiness system to pass by. The 2½° signal is therefore transport-dominated, and its autocorrelation is consequently very model-dependent. By contrast, the autocorrelation of an area much *longer* than the 20° advection length, such as curve 8 in Fig. 5b, satisfies the criterion $d \gg v\tau_L$, and therefore decays according to (A4) in a time relatively insensitive to transport.

REFERENCES

Bell, T. L., 1980: Climate sensitivity from fluctuation-dissipation: Some simple model tests. *J. Atmos. Sci.*, **37**, 1700–1707.

Bertoni, E. A., and I. A. Lund, 1963: Space correlations of the height of constant pressure surfaces. *J. Appl. Meteor.*, **2**, 539–545.

Chang, C.-P., 1970: Westward propagating cloud patterns in the tropical Pacific as seen from time-composite satellite photographs. *J. Atmos. Sci.*, **27**, 131–138.

Coffey, M. T., 1977: Water vapor absorption in the 10–12 μm atmospheric window. *Quart. J. Roy. Meteor. Soc.*, **103**, 685–692.

Environmental Satellite Imagery, NOAA 1972: *Key to Meteorological Records Documentation.* No. 5.4, National Oceanic and Atmospheric Administration, Environmental Data Services (available from NTIS).

Fisher, M. J., and P. O. A. L. Davies, 1964: Correlation measurements in a non-frozen pattern of turbulence. *J. Fluid Mech.*, **18**, 97–116.

Gandin, L. S., 1963: *Objective Analysis of Meteorological Fields.* Gidrometeor. Izdatel., Leningrad [Translated from Russian, Israel Program for Scientific Translations, Jerusalem, 1965, 242 pp.].

Gruber, A., and J. S. Winston, 1978: Earth-atmosphere radiative heating based on NOAA scanning radiometer measurements. *Bull. Amer. Meteor. Soc.*, **59**, 1570–1573.

Hartmann, D. L., and D. A. Short, 1980: On the use of earth radiation budget statistics for studies of clouds and climate. *J. Atmos. Sci.*, **37**, 1233–1250.

Hayden, C. M., 1970: An objective analysis of cloud cluster dimensions and spacing in the tropical North Pacific. *Mon. Wea. Rev.*, **98**, 534–540.

Heddinghaus, T. R., and A. F. Krueger, 1981: Annual and interannual variations in outgoing longwave radiation over the tropics. *Mon. Wea. Rev.*, **109**, 1208–1218.

King, M. D., and R. J. Curran, 1980: The effect of a nonuniform planetary albedo on the interpretation of Earth radiation budget observations. *J. Atmos. Sci.*, **37**, 1262–1278.

Leith, C. E., 1973: The standard error of time average estimates of climatic means. *J. Appl. Meteor.*, **12**, 1066–1069.

Leith, C. E., 1975: Climate response and fluctuation-dissipation. *J. Atmos. Sci.*, **32**, 2022–2026.

Murakami, T., 1980a: Empirical orthogonal function analysis of satellite-observed outgoing longwave radiation during summer. *Mon. Wea. Rev.*, **108**, 205–222.

——, 1980b: Temporal variations of satellite observed outgoing longwave radiation over the winter monsoon region. Part I: Long period (15–30) oscillations. *Mon. Wea. Rev.*, **108**, 408–426.

——, 1980c: Temporal variations of satellite-observed outgoing longwave radiation over the winter monsoon region. Part II: short period (4–6 days) oscillations. *Mon. Wea. Rev.*, **108**, 427–444.

North, G. R., R. F. Cahalan, and J. A. Coakley, Jr., 1981: Energy balance climate models. *Rev. Geophys. Space Phys.*, **19**, 91–121.

——, and ——, 1981: Predictability in a solvable stochastic climate model. *J. Atmos. Sci.*, **38**, 504–513.

Ohring, G., and P. Clapp, 1980: The effect of changes in cloud amount on the net radiation at the top of the atmosphere. *J. Atmos. Sci.*, **37**, 447–454.

Reed, R. J., 1979: Cyclogenesis in polar air streams. *Mon. Wea. Rev.*, **107**, 38–52.

——, and E. E. Recker, 1971: The structure and properties of synoptic-scale wave disturbances in the equatorial western Pacific. *J. Atmos. Sci.*, **28**, 1117–1133.

Riehl, H., and A. H. Miller, 1978: Differences between morning and evening temperatures of cloud tops over tropical continents and oceans. *Quart. J. Roy. Meteor. Soc.*, **104**, 757–764.

Roberts, R. E., J. E. A. Selby and L. M. Biberman, 1976: Infrared continuum absorption by atmospheric water vapor in the 8–12 μm window. *Appl. Opt.*, **15**, 2085–2090.

Schlichting, H., 1968: *Boundary-Layer Theory.* McGraw-Hill, 748 pp. (see p. 536).

Short, D. A., and J. M. Wallace, 1980: Satellite-inferred morning-to-evening cloudiness changes. *Mon. Wea. Rev.*, **108**, 1160–1169.

Streten, N. A., and A. J. Troup, 1973: A synoptic climatology of satellite observed cloud vortices over the Southern Hemisphere. *Quart. J. Roy. Meteor. Soc.*, **99**, 56–72.

Wallace, J. M., and L. A. Chang, 1972: On the application of satellite data on cloud brightness to the study of tropical wave disturbances. *J. Atmos. Sci.*, **29**, 1400–1403.

Webster, P. J., 1981: Mechanisms determining the atmospheric response to sea surface temperature anomalies. *J. Atmos. Sci.*, **38**, 554–571.

Williams, K. T., and W. M. Gray, 1973: Statistical analysis of satellite observed trade wind cloud clusters in the western North Pacific. *Tellus*, **25**, 313–336.

Winston, J. S., and A. F. Krueger, 1977: Diagnosis of the satellite-observed radiative heating in relation to the summer monsoon. *Pure Appl. Geophys.*, **115**, 1131–1144.

Zangvil, A., 1975: Temporal and spatial behavior of large-scale disturbances of tropical cloudiness deduced from satellite brightness data. *Mon. Wea. Rev.*, **103**, 904–920.